Article

Terbium (III) Oxide (Tb₂O₃) Transparent Ceramics by Two-Step Sintering from Precipitated Powder

Dianjun Hu [1,2], Xiaoying Li [1,2], Lixuan Zhang [1,2], Ilya Snetkov [3,4], Penghui Chen [1,2], Zhengfa Dai [1], Stanislav Balabanov [5], Oleg Palashov [3,4] and Jiang Li [1,2,*

[1]   Transparent Ceramics Research Center, Shanghai Institute of Ceramics, Chinese Academy of Sciences, Shanghai 201899, China; hudianjun@student.sic.ac.cn (D.H.); lixiaoying19@mails.ucas.ac.cn (X.L.); zhanglixuan@student.sic.ac.cn (L.Z.); chenpenghui20@mails.ucas.ac.cn (P.C.); daizhengfa@mail.sic.ac.cn (Z.D.)

[2]   Center of Materials Science and Optoelectronics Engineering, University of Chinese Academy of Sciences, Beijing 100049, China

[3]   Institute of Applied Physics, Russian Academy of Sciences, 46 Uljanov Str., 603950 Nizhny Novgorod, Russia; snetkov@appl.sci-nnov.ru (I.S.); opalopalopal@yandex.ru (O.P.)

[4]   Research Institute for Physics and Technology, Lobachevsky State University of Nizhny Novgorod, 23 Gagarin Ave., 603950 Nizhny Novgorod, Russia

[5]   G.G. Devyatykh Institute of Chemistry of High-Purity Substances, Russian Academy of Sciences, 49 Tropinin Str., 603951 Nizhny Novgorod, Russia; stanislav.s.balabanov@gmail.com

*   Correspondence: lijiang@mail.sic.ac.cn; Tel.: +86-21-69163689; Fax: +86-21-69906700

Abstract: As a result of preliminary air calcination and subsequent reduction in a flowing NH_3 atmosphere of the precursor from the liquid precipitation method for the first time, pure-phase Tb_2O_3 powder with an average particle size of 135 nm was prepared. The Tb_2O_3 magneto-optical transparent ceramics with the average grain size of 1.3 μm were successfully fabricated by vacuum pre-sintering and hot isostatic pressing post-treatment from the as-synthesized Tb_2O_3 powder. In-line transmittance values of Tb_2O_3 ceramics reach 70.3% at 633 nm, 78.1% at 1064 nm, and 79.4% at 1400 nm, respectively. Thanks to the high intrinsic concentration of Tb^{3+}, Tb_2O_3 ceramics present high Verdet constants of -427.3 and -123.7 rad·T^{-1}·m^{-1} at 633 and 1064 nm, which are about 3.1 and 3.4 times higher than those of commercial $Tb_3Ga_5O_{12}$ crystals, respectively. Due to the excellent magneto-optical properties, Tb_2O_3 ceramics are promising candidates for the development of Faraday isolator toward compaction used in visible and near-infrared bands.

Keywords: Tb_2O_3 transparent ceramics; liquid precipitation; two-step sintering; magneto-optical properties

1. Introduction

After the discovery of the Faraday effect in 1845, magneto-optical effects such as the Kerr effect in 1876, Zeeman effect in 1896 and Cotton–Mouton effect in 1907 have been discovered in succession [1–3]. As a result, a variety of magneto-optical materials, which own the magneto-optical properties, have emerged and developed subsequently, and these are applied universally in optical communication, optical fiber current sensor [4], optical isolator [5–8] and other magneto-optical devices. As one of the magneto-optical effects, the Faraday effect, which can make the polarization plane of the transmitted light nonreciprocally deflect, is widely applied in the optical isolator of lasers to ensure laser unidirectional passing and block the reverse light effectively. The traditional Faraday isolator magneto-optical materials mainly composed of glasses [9,10] and crystals [11] have been developed and progressed to the practical application with the development of the laser system. Recently, with the rapid development of the advanced processing technologies of transparent ceramics, the advantages of transparent ceramics in mechanics, optics, thermal properties and other aspects are increasingly prominent [12,13], which also provides a novel thought for the development of transparent magneto-optical ceramics that can be

applied in Faraday isolators [14]. Transparent ceramics have been considered to be the most promising candidates to substitute the single crystals and glasses in Faraday isolators.

The early reported magneto-optical ceramic materials are mainly in garnet structures, such as $Tb_3Ga_5O_{12}$ (TGG) [15–20] and $Tb_3Al_5O_{12}$ (TAG) [21–27]. In recent years, there have been some research reports on sesquioxide magneto-optical ceramics with a larger Verdet constant than the corresponding garnet structure as a result of the high intrinsic concentration of magnetically active rare earth ions, such as terbium oxide (Tb_2O_3) [28–32], holmium oxide (Ho_2O_3) [33–37], dysprosium oxide (Dy_2O_3) ceramics [38–42], etc. Among them, the Verdet constant of Tb_2O_3 at 380–1750 nm, which is the highest Verdet constant as known so far, is over three times that of commercial TGG single crystals. Nevertheless, the oxidation when heated in air and the reversible phase transition above 1600 °C of Tb_2O_3 bring some problems to the growth of single crystals [43] and the fabrication of Tb_2O_3 ceramics. One of the effective methods to obtain Tb_2O_3-based ceramics is through the preparation of solid solution of Tb_2O_3 and other RE_2O_3 such as Y_2O_3 and Lu_2O_3. Snetkov et al. [28] prepared $Tb^{3+}:Y_2O_3$ ceramics with Tb^{3+} doping concentrations of 10%, 20%, 30%, and 100% (pure Tb_2O_3) by hot pressing (HP) from the self-propagating high temperature synthesis (SHS) powders. It was found that the Verdet constant of $Tb^{3+}:Y_2O_3$ ceramics increased linearly with the rise of Tb^{3+} concentration. The $30\%Tb^{3+}:Y_2O_3$ ceramics had an equivalent Verdet constant to TGG single crystals containing 37.5 at % Tb^{3+}, and the pure Tb_2O_3 ceramics had a substantially higher value of the Verdet constant in the entire wavelength range. Ikesue et al. [29,30] successfully fabricated high-quality magneto-optical ceramics $(Tb_xY_{1-x})_2O_3$ (x = 0.5−1.0) (TYO) by vacuum sintering with subsequent hot isostatic pressing (HIP) treatment using the commercial powders. The pure Tb_2O_3 ceramics showed the highest value of the Verdet constant: 3.8 times higher than that of the commercial TGG. Yang et al. [44] prepared the $(Tb_{0.5}Y_{0.5})_2O_3$ transparent ceramics by flowing H_2 sintering from co-precipitation synthesis powders. The transmittance reached 71.9% at 1400 nm, and the Verdet constant at 633 nm was only 1.64 times that of TGG single crystals. Zhang et al. [45] investigated the phase transformation process of Tb_2O_3 when heated in different atmosphere, providing a deep understanding of controlling and avoiding the phase transformations of Tb_2O_3. The $(Tb_{1-x}Lu_x)_2O_3$ ceramics were then fabricated and had a Verdet constant of -244.33 rad·T^{-1}·m^{-1} at 633 nm, which was 30% higher than that of $Tb_3Al_5O_{12}$ materials [32]. These reports indicate that Tb_2O_3 ceramics have optical properties well suited for Faraday isolators, and because of the large Verdet constant, Tb_2O_3 ceramics can further reduce the size of Faraday isolator devices.

The introduction of Y_2O_3 or Lu_2O_3 and the formation of solid solution have been proved to effectively stabilize the lattice structure of Tb_2O_3 cell, preventing the oxidation and raising the phase transition temperature of Tb_2O_3. However, the occupation of non-magnetic active ions such as Y^{3+} or Lu^{3+} results in the obvious decrease in Verdet constant. In addition to the method of the preparation of solid solution, by using the nano-powder with high sintering activity and sintering aids, there is a great possibility to prepare the pure Tb_2O_3 ceramics below the phase transition temperature. Balabanov et al. [31,46] successfully fabricated $RE:Tb_2O_3$ ceramics ($RE-Y^{3+}$, Lu^{3+}, Sc^{3+}, Ce^{3+}, Dy^{3+}, Ho^{3+}, Yb^{3+}, Nd^{3+}) by HP using the SHS powders. The absolute value of Verdet constant of $RE:Tb_2O_3$ ceramics decreased with the introduction of RE ions in relatively high concentration. ZrO_2 has been demonstrated to be an effective sintering aid for inhibiting grain growth during the sintering period [30]. In this paper, high sintering activity Tb_2O_3 nano-powder was synthesized via the precipitation method. Without RE ion dopant, pure Tb_2O_3 ceramics with high optical quality and high Verdet constant were obtained after vacuum pre-sintering and the following HIP post-treatment both below the phase transition temperature. The composition and thermal decomposition evolution of the precursor were studied. The optical transmittance and microstructure of Tb_2O_3 ceramics were investigated. In addition, the wavelength dependence of the Verdet constant of the Tb_2O_3 ceramics at room temperature was identified in detail.

2. Materials and Methods

2.1. Materials

Tb_4O_7 (99.99%, Yuelong Rare Earth New Materials Co., Ltd., Shanghai, China), NH_4HCO_3 (99.995%, Aladdin Industrial Corporation, Shanghai, China), $(NH_4)_2SO_4$ (Analytical grade, Sinopharm Chemical Reagent Co., Ltd., Shanghai, China), high-purity concentrated nitric acid (G3, Shanghai Aoban Technology Co., Ltd., Shanghai, China) and $ZrOCl_2 \cdot 8H_2O$ (99.5%, Jining Zhongkai New Materials Co., Ltd., Jining, China) were used as raw materials.

2.2. Methods

The positive strike precipitation method was employed for the preparation of Tb_2O_3 nano-powder. Firstly, Tb_4O_7 powder was dissolved in a high-purity concentrated nitric acid with stirring and heating to obtain a $Tb(NO_3)_3$ solution. After the complete dissolution of Tb_4O_7 powder, the solution was filtered for the separation of insoluble impurities. The chemical analysis was then applied to assay the concentration of the $Tb(NO_3)_3$ solution. $(NH_4)_2SO_4$ was dissolved in ultrapure water as the dispersant with 1.0 mol/L concentration. NH_4HCO_4 was also dissolved in ultrapure water to obtain the precipitation solution (concentration of 1.0 mol/L). The zirconia source was from $ZrOCl_2 \cdot 8H_2O$ via dissolving in ultrapure water (concentration = 0.1 mol/L). In this paper, a novel method is proposed for a more uniform introduction of ZrO_2 by liquid co-precipitation synthesis rather than conventional ball milling, which can simplify the process procedure and avoid the introduction of unnecessary impurities.

Firstly, $(NH_4)_2SO_4$ solution was added to the mixed metal ions solution as a dispersant with the ratio of $n(Tb^{3+})/n((NH_4)_2SO_4)$ equal to 1:1. The mixed solution was diluted with deionized water to 500 mL with the concentration of Tb^{3+} to be 0.2 mol/L. In the process of precipitation, 400 mL of NH_4HCO_3 precipitant solution was dripped into 500 mL of mixed aqueous solution of $Tb(NO_3)_3$, $(NH_4)_2SO_4$ and $ZrOCl_2$ at the speed of 3 mL/min under stirring, with the pH of the reaction solution increasing from 0.98 to 6.48. Subsequently, the obtained precipitate slurry was aged for 4 h at room temperature without any disturbance. Finally, the resultant suspension was filtered and washed repeatedly with deionized water and absolute alcohol to remove by-products.

After drying at 70 °C for 36 h and sieving with a 200 screen mesh, the resultant precursors were obtained. After the preliminary air calcination at 1100 °C for 4 h and subsequently novel reduction in a flowing reducing atmosphere of NH_3 at 1250 °C with a holding time of 4 h, white Tb_2O_3 powder was obtained. The Tb_2O_3 powder was dry pressed at 40 MPa and then cold isostatic pressed (CIP) at 250 MPa to obtain green bodies. The compacted pellets were vacuum pre-sintered at 1550 °C for 3 h and then HIP post-treated at 1450 °C for 3 h under 150 MPa Ar atmosphere. Finally, the Tb_2O_3 ceramics were mirror-polished on both sides to the thickness of 1.0 mm.

2.3. Characterization

The thermal decomposition behavior of the precursor was analyzed by the thermogravimetry and differential thermal analysis (TG-DTA, STA449 F3, Netzsch, Bavaria, Germany) from room temperature to 1100 °C in air with a heating rate of 10 °C/min. The phases of the synthesized precursor, the calcined powder and the reduced powder were identified by the X-ray diffraction (XRD, D8 Advance, Bruker AXS GMBH, Karlsruhe, Germany) using Cu K_α radiation (λ = 0.15418 nm) in the range of 2θ = 20–80°. The morphologies of these powders were measured by the field emission scanning electron microscopy (FESEM, SU9000, Hitachi, Tokyo, Japan), and the mean particle size was estimated by measuring the diameters of at least 300 particles in the FESEM micrographs. The microstructures of the Tb_2O_3 ceramics were investigated by a field emission scanning electron microscopy (FESEM, Magellan 400, FEI, Hillsboro, OR, USA). The average grain size of Tb_2O_3 ceramics was measured by using a statistical method, thanks to the Nano Measure software, with at least 500 grains counted. The in-line transmittances of the mirror-polished

Tb_2O_3 ceramics (thickness = 1.0 mm) were measured by a UV-VIS-NIR spectrophotometer (Model Cray-5000, Varian, CA, USA) in 300–1400 nm range. The polarization extinction method was used to measure the Verdet constant of the Tb_2O_3 ceramics in this work. Specifically, two measurement techniques were carried out to measure the wavelength dependence of the Verdet constant: (1) using probe laser sources, 405, 532, 658, 808, 980, and 1064 nm diodes and 632.8 nm He-Ne laser were utilized as probe laser radiation sources; (2) using the polarization stepping method, as described in Refs. [37,47]. According to the formula of Faraday rotation angle: $\theta = VBd$, the Verdet constant (V) can be shown as: $V = \theta/(B \cdot d)$, where θ defines the Faraday rotation angle, V represents the Verdet constant, B shows the applied magnetic field, and d donates the length of magneto-optical materials (d = 2.0 mm).

3. Results and Discussion

Figure 1 presents the TG-DTA-DTG curves of the as-synthesized precursor. The values consisting of a DTG curve are from the first derivative of the TG curve, which can help to clearly distinguish each thermal decomposition stage. The thermal decomposition process of the precursor with the total weight loss of 26.7% can be divided into four main stages. The weight loss of about 3.4% below 141 °C is derived from the removal of residual ethanol, absorbed water and partial crystallized water, and the endothermic peak is centered at about 73 °C. The weight loss of 7.5% in the second stage from 141 to 313 °C is ascribed to the removal of ammonium radical and the dehydration, and the endothermic pick located at 258 °C is mainly assigned to the dehydration of the O-H groups and the removal of residual water. The weight loss of about 15.1% between 313 and 900 °C is the result of the further dehydration of the O-H groups and the decomposition of carbonate. No significant weight loss happens between 850 and 900 °C, implying that the precursor has almost decomposed into terbium oxide and mainly in the form of $TbO_{1.714}$ (Tb_7O_{12}) phase [45]. There is a slight weight loss about 0.7% between 900 and 1000 °C, deriving from the decomposition of sulfate as well as the deoxidization reaction of terbium oxide from $TbO_{1.714}$ to $TbO_{1.5}$ according to Ref. [45], and the corresponding endothermic peak is situated at near 930 °C. No obvious weight loss is observed above 1000 °C, presenting that the carbonate and sulfate in the synthesized precursor have been decomposed completely after 1000 °C.
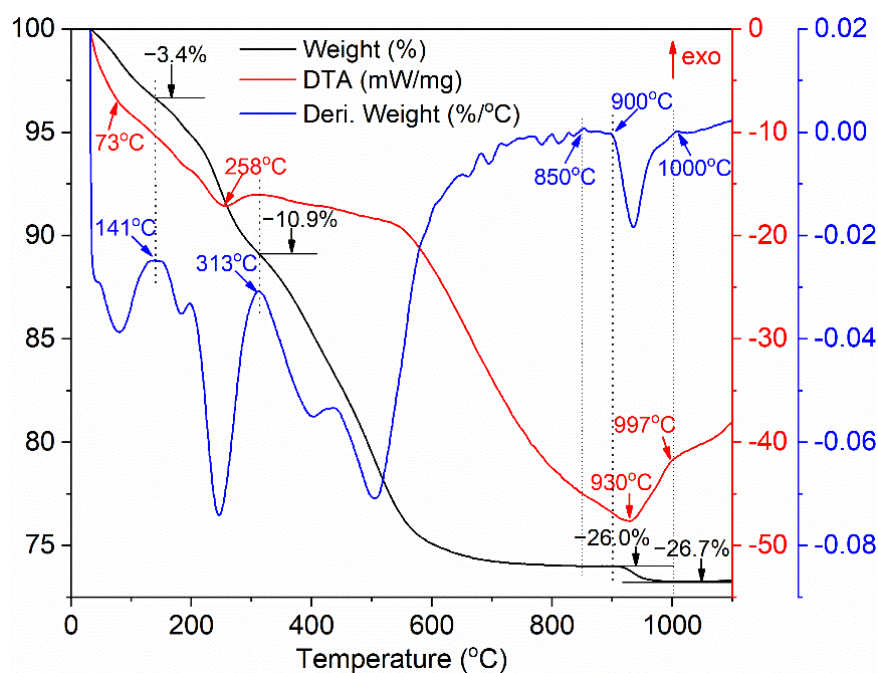

Figure 1. TG-DTA-DTG curves of the synthesized precursor.

Figure 2 shows the FTIR spectrum of synthesized precursor. The precursor shows a wide absorption band from 3700 to 2640 cm^{-1} and centered at about 3400 cm^{-1}, which is relevant to the stretching vibration of free OH$^-$ groups (about 3000–3700 cm^{-1}) and the bending vibration of H-O-H from the molecules water in the precursor (symmetric ν_1 and anti-symmetric ν_3, 3200–3500 cm^{-1}) [48]. The 1628 cm^{-1} shoulder is originated from the bending mode (ν_2) of the H-O-H [49]. These peaks at 1508, 1416, 1086, 836, 760 and 688 cm^{-1} are all bound up with the existence of CO$_3^{2-}$. Two absorption peaks in the regions of 1508 cm^{-1} (asymmetric ν_3) and 1416 cm^{-1} (symmetric ν_3) are defined as the stretching mode of the C-O bond in CO$_3^{2-}$ groups [50]. The splitting at this band can be ascribed to carbonate ions located at a crystallographically non-equivalent site [51,52]. The peak centered at 1086 cm^{-1} is characteristic of the ν_1 symmetric stretch of CO$_3^{2-}$, which may overlap the weak peak of SO$_4^{2-}$ located at about 1100 cm^{-1}. These peaks at 836, 760 and 688 cm^{-1} are assigned to the δ out-of-plane bending vibration, ν_3 and ν_6 vibration of CO$_3^{2-}$, respectively [52,53]. Based on the above analysis, the precursor is the terbium hydroxycarbonate with crystal water [53].
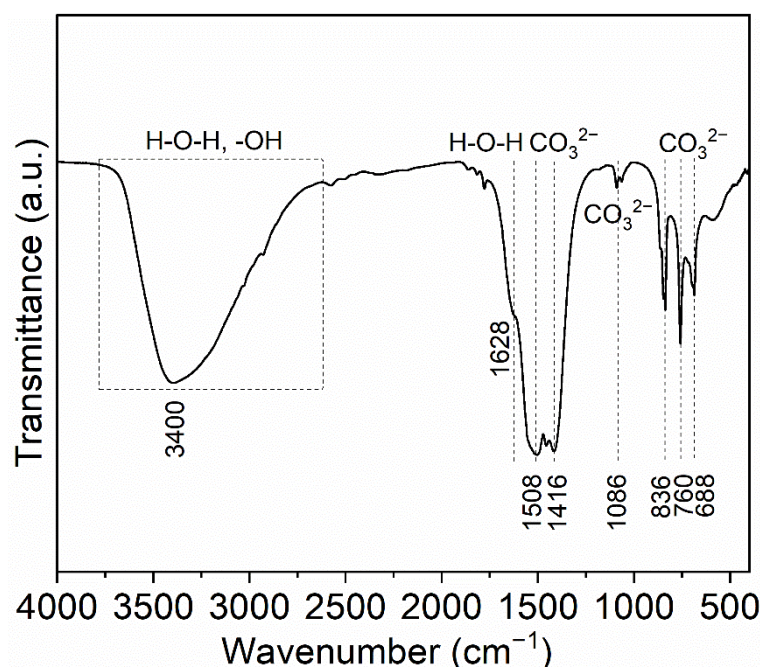

Figure 2. FTIR spectrum of the synthesized precursor.

A novel treatment method of air calcination and NH$_3$ reduction is adopted to obtain pure Tb$_2$O$_3$ nano-powder. The as-synthesized precursor was firstly calcined at 1100 °C for 4 h in air to completely remove the carbonate and sulfate in the precursor, avoiding the possible residue of carbon or sulfur, which was hardly removed by the subsequent sintering under an oxygen-free environment. The resultant dark brown powder was subsequently reduced at 1250 °C for 4 h in a flowing reducing NH$_3$ atmosphere to obtain white Tb$_2$O$_3$ powder. Figure 3 displays the XRD patterns of the precursor, the calcined and the reduced powders. The precursor presents a certain crystallinity. Unfortunately, there is no corresponding standard card in the database. After calcination at 1100 °C for 4 h in air, the main diffraction peaks of the calcined powder are well consistent with the standard patterns of Tb$_7$O$_{12}$ (trigonal, R-3(148), PDF#34-0518) and Tb$_{11}$O$_{20}$ (triclinic, P-1(2), PDF#65-4511) intermediate phases [54]. The air calcined powder is proved to be the mixture of Tb$_7$O$_{12}$ (2Tb$_2$O$_3$·3TbO$_2$) and Tb$_{11}$O$_{20}$ (2Tb$_2$O$_3$·7TbO$_2$) phases with coexisting trivalent and tetravalent oxidation states, rather than the Tb$_2$O$_3$ phase as illustrated in Figure 1, due to the oxidization of Tb$_2$O$_3$ during the cooling process in air. The Tb$_2$O$_3$ phase with only a trivalent oxidation state is unstable both during the heating and cooling process in air, and an oxygen-free atmosphere is necessary for the fabrication of Tb$_2$O$_3$

ceramics. The similar XRD patterns of powder are also presented for the powder prepared by SHS in air [46,55]. Reducing of the air calcined powder in a flowing of NH_3 atmosphere results in the reduction of terbium ions converting to the trivalent state. The diffraction peaks of the reduced powder are in good accordance with the diffraction pattern of cubic phase Tb_2O_3 (Ia-3(206), PDF#65-3180), and no impurities or secondary phases are observed, meaning that the precursor can be effectively converted to Tb_2O_3 powder with a cubic structure after air calcination and NH_3 reduction. It is the first time that pure phase Tb_2O_3 powder is synthesized by the liquid precipitation method followed by air calcination and subsequent NH_3 reduction to the best of our knowledge. The Tb_2O_3 powder displays a better crystallinity than the calcined powder according to the narrower diffraction peaks. The corresponding average crystalline size (D_{XRD}) can be figured out through the Scherrer formula [56]:

$$D_{XRD} = 0.89\lambda/(\beta \cdot \cos\theta), \tag{1}$$

where λ is on behalf of the K_α radiation wavelength of the Cu target (λ = 1.542 Å), β represents the full width at half-maximum (FWHM) of the diffraction peak, and θ is the Bragg angle. The calculated result D_{XRD} of Tb_2O_3 powder is 59 nm. The combination of liquid precipitation synthesis and air calcination as well as NH_3 reduction is strongly recommended for the preparation of Tb_2O_3 nano-powder.
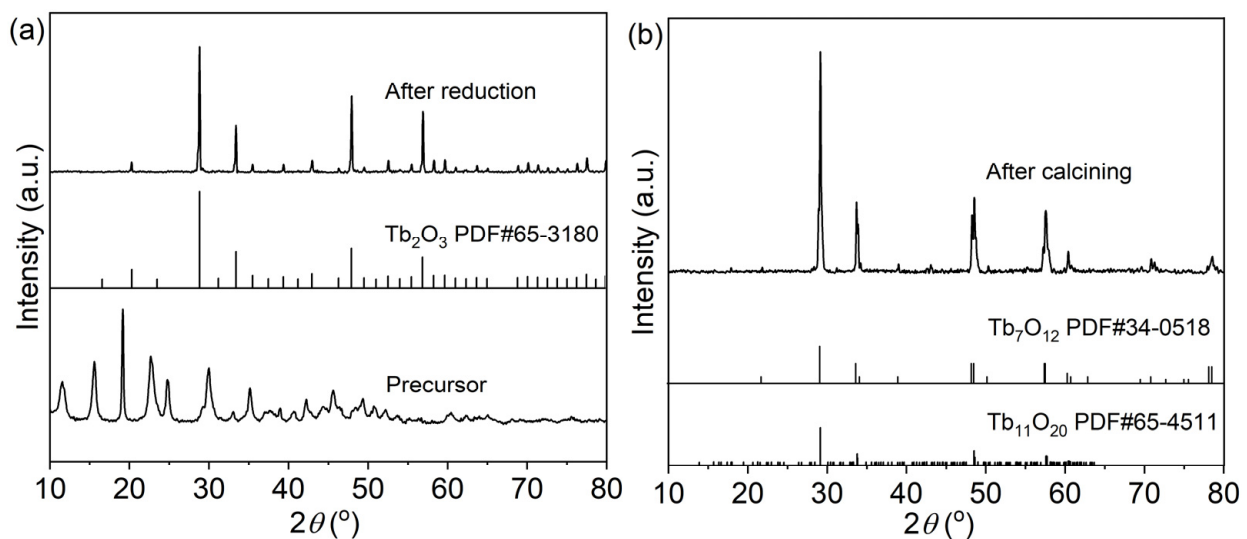

Figure 3. XRD patterns of the precursor and reduced powder (**a**), and the calcined powder (**b**).

Figure 4 displays the FESEM micrographs of the as-synthesized precursor, the calcined powder and the Tb_2O_3 powder. The precipitated precursor presents a two-dimensional needle or flake structure with a thickness of several nanometers and a length of several hundred nanometers, as shown in Figure 4a, and the precursor is relatively loose and slightly agglomerated. After heat treatment, the morphology of the powder changes greatly, and the precursor is fully collapsed into the uniform particles. The air calcined powder and Tb_2O_3 powder after reduction treatment have the similar morphologies and consist of near-spherical primary particles. It is noticed that sintering necks appear between powders, implying that a slight sintering phenomenon occurs between powders. According to the FESEM micrograph in Figure 4c, the particle size of the Tb_2O_3 powder is roughly counted, and the particle size distribution can be appreciated more quantitatively in Figure 4d. It can be figured out that the Tb_2O_3 powder shows a narrow particle size distribution. The particle size of the obtained Tb_2O_3 powder is principally distributed in the range of 60–180 nm, in which the range of 100–120 nm accounts for the largest proportion. The obtained Tb_2O_3 powder with the average particle size of about 135 nm and a unimodal particle-size distribution helps to realize the uniform densification and reduce the coordination number

of pores during the ceramic sintering process, and it is instrumental in the preparation of transparent ceramics with high quality.
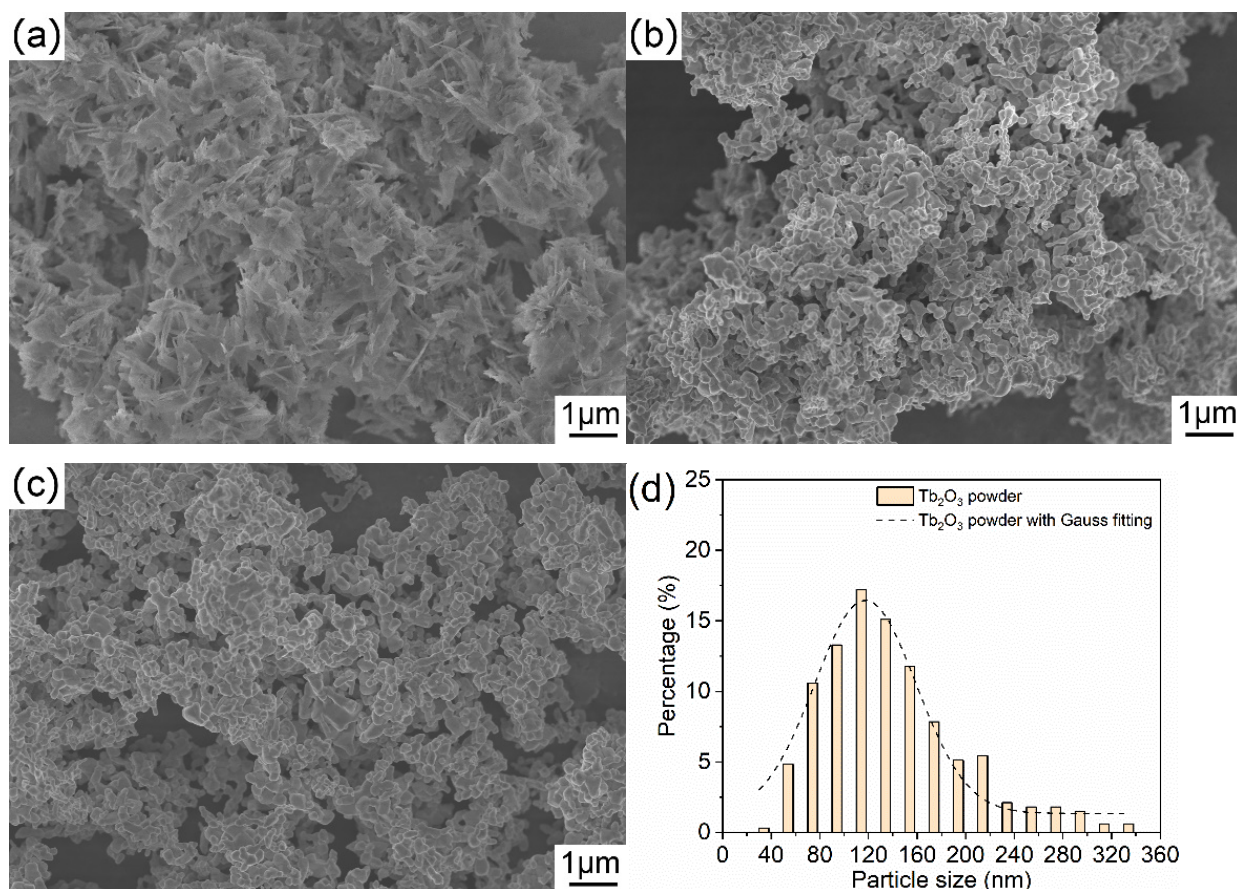

Figure 4. FESEM images of the precursor (**a**), the air calcined powder (**b**), the Tb_2O_3 powder (**c**), and the particle size distribution histogram of the Tb_2O_3 powder (**d**).

Using the synthesized Tb_2O_3 powder, Tb_2O_3 transparent ceramics were successfully obtained by the subsequent two-step sintering schedule consisting of vacuum pre-sintering at 1550 °C for 3 h and HIP post-treatment at 1450 °C for 3 h under 150 MPa Ar atmosphere. Figure 5 shows the in-line transmission curve from the visible to near-infrared wavelength range and the appearance of the Tb_2O_3 ceramics with 1.0 mm thickness after double-side polishing. The Tb_2O_3 ceramics exhibit relatively good transparency in the visible to near-infrared wavelength range. The in-line transmittance values are about 70–80% in the 600–1400 nm wavelength range, and the values reach 79.4% at the wavelength of 1400 nm, 78.1% at 1064 nm, and 70.3% at 633 nm, respectively (the theoretical transmission ≈80.1%). There is a slight decrease in the in-line transmittance with the decrease in wavelength, particularly in the short-wavelength region, which implies the Rayleigh scattering inside the sample. In addition, oxygen vacancy derived from the weak reducing environment during vacuum pre-sintering and the HIP post-treatment period also plays the role of absorption center and brings about the decrease in transmittance. The cutoff edge is situated at about 346 nm. The relatively strong absorption peak centered at 484 nm is attributed to the $^7F_6 \rightarrow ^5D_4$ transition of Tb^{3+}.
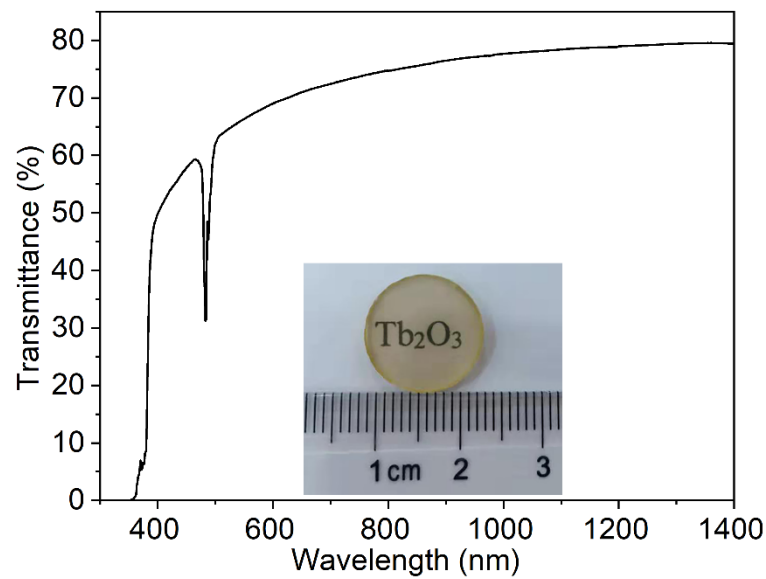
Figure 5. Photograph and in-line transmission curve of the synthetic Tb_2O_3 ceramics (thickness = 1.0 mm).

Figure 6 shows the microstructure of the Tb_2O_3 transparent ceramics and the grain size distribution. It is discovered that the Tb_2O_3 ceramics consist of uniform grains with different crystal orientations, and no secondary phase or abnormal growth is observed. There are a very few intergranular closed pores of nano-size seated at the trigeminal grain boundaries, which lead to the slight reduction in the in-line transmittance in the visible range. The grain boundaries are very clear and clean. It is also notable that the polishing post-treatment for the Tb_2O_3 ceramics is a bit rough, and there are many scratches on the polished surface of the Tb_2O_3 ceramics, which also bring out the decrease in the measured values of in-line transmittance. The grain size distribution and the cumulative percentage are displayed in the histogram in Figure 6b. Statistical values of the grain size of Tb_2O_3 ceramics predominantly range from 0.8 to 1.6 μm with the largest proportion range being 1.2–1.4 μm. The statistic average grain size of the Tb_2O_3 ceramics is approximately 1.3 μm, which is far smaller than the reported values.
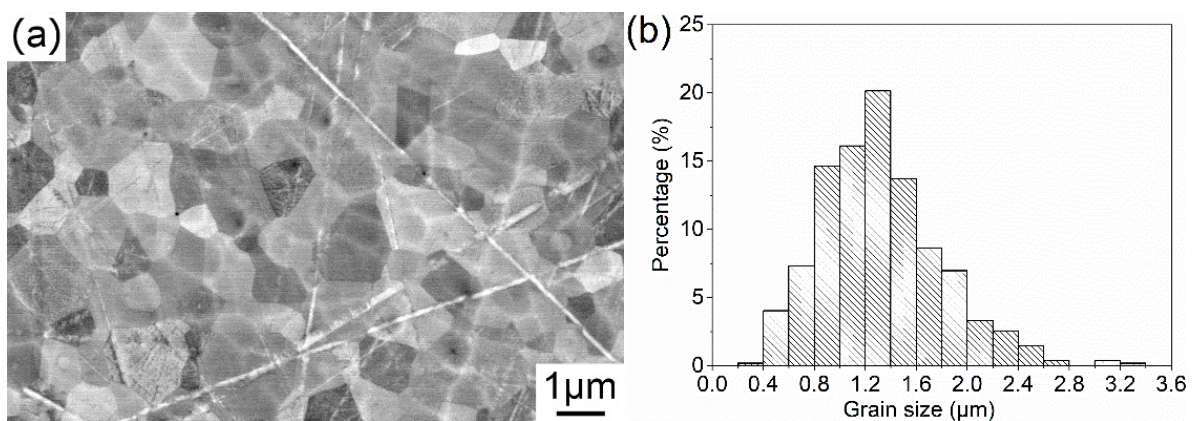

Figure 6. FESEM micrograph of the surface of Tb_2O_3 ceramics (**a**) and the grain size distribution (**b**).

Magneto-optical materials with a large Verdet constant can be realized through containing a high intrinsic concentration of magnetically active rare-earth ions such as Dy^{3+}, Tb^{3+} and Ho^{3+}, which are paramagnetic and possess large magnetic moments because of

the electronic transition $4f^n \rightarrow 4f^{n-1}5d$. A Van Vleck–Hebb equation is usually applied to figure out the Verdet constant of rare-earth ions doped materials [7,9,57]

$$V = \frac{4\pi^2 N v^2 \mu_{eff}^2}{3chkTg\mu_B} \sum_n \frac{C_n}{v^2 - v_n^2}, \qquad (2)$$

where c represents the speed of light, h means Planck constant, k indicates Boltzmann constant, T implies temperature, g is the Lande splitting factor, μ_B displays the Bohr magneton number, N shows the paramagnetic ion concentration, μ_{eff} is the effective magnetic moment, v expresses the light frequency, v_n is the frequency related to the excited state, and C_n denotes the transition moments, respectively. When talking about the paramagnetic rare-earth ions, Equation (2) can be reducible to a single oscillator model to illustrate the wavelength dependence of the Verdet constant, which is in the form as shown below [57]:

$$1/V = a\left(\lambda^2 - \lambda_0^2\right), \qquad (3)$$

where a and λ_0 are approximation parameters. λ_0 is the effective transition wavelength of the rare earth ion. Constant a is independent of the wavelength and determined by the concentration of paramagnetic ions, the refractive index of the material and the effective transition probability [31]. Theoretically, the inverse of the Verdet constant $1/V$ is proportional to λ^2 according to Equation (3).

The Verdet constants of the Tb_2O_3 ceramics are measured by probe laser sources and by the "polarization stepping" method in this work, and the difference between the values of Verdet constant measured by the two methods are both less than 4% at 633 and 1064 nm. The measured values of the Verdet constant at some certain wavelengths are presented in Table 1. Tb_2O_3 transparent ceramics show more than 3 times higher values of the Verdet constant than TGG single crystals in the whole wavelength range, and the advantage is not monotonic, decreasing from 3.6 times at 405 nm ($V(Tb_2O_3) = -1620.8$ rad·T^{-1}·m^{-1}, $V(TGG) = -453.2$ rad·T^{-1}·m^{-1}) to 3.0 times at 658 nm ($V(Tb_2O_3) = -369.3$ rad·T^{-1}·m^{-1}, $V(TGG) = -122.1$ rad·T^{-1}·m^{-1}) and then further increasing to 3.4 times at 1064 nm ($V(Tb_2O_3) = -123.7$ rad·T^{-1}·m^{-1}, $V(TGG) = -36.7$ rad·T^{-1}·m^{-1}).

Table 1. Verdet constants of Tb_2O_3 ceramics at different wavelengths and the Verdet constants of TGG crystal in Ref. [58] for comparative measurement.

Wavelength (nm)	V(Tb_2O_3) in Absolute Value (Rad·T^{-1}·m^{-1})	V(TGG) in Absolute Value (Rad·T^{-1}·m^{-1})	V(Tb_2O_3)/V(TGG)
405	1620.8	453.2	3.6
532	672.4	196.5	3.4
633	427.3	136.2	3.1
658	369.3	122.1	3.0
808	235.0	74.8	3.1
980	150.1	48.7	3.1
1064	123.7	36.7	3.4

The inverse of the Verdet constant as a function of λ^2 for the Tb_2O_3 ceramics is plotted in Figure 7 in light of Equation (3). There is an apparent positive linear correlation between $1/V$ and λ^2, according to Figure 7, which is consistent with the Van Vleck–Hebb single oscillator model in the visible and near-infrared range. The effective transition wavelength λ_0 of the Tb^{3+} ion and the wavelength independent constant a for the Tb_2O_3 ceramics are obtained by fitting the experimental results in Table 1 (the absolute values of the Verdet constant at different wavelengths). The effective transition wavelength λ_0 is approximately 299 nm, corresponding to the $4f^8 \rightarrow 4f^7 5d$ transition of the Tb^{3+} ion. λ_0 can marginally change in different materials in theory, which is due to the fact that the energy levels of the rare-earth ions differ in different materials. The coefficient a is fitted to be

0.00769 (T·m)/(rad·μm^2) with the matching factor R^2 equal to 0.999 for Tb_2O_3 ceramics in this work, which is within the range of linear behavior.
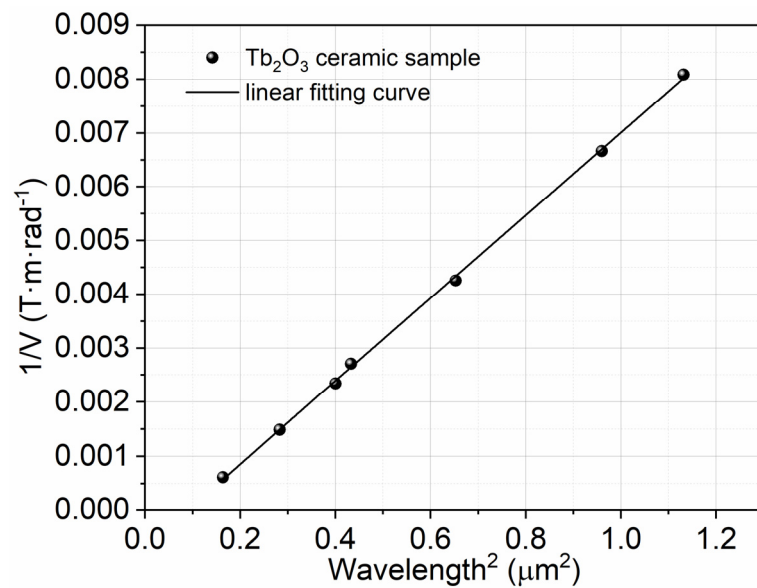

Figure 7. Inverse of the Verdet constant (1/V) as a function of squared wavelength (λ^2) for the Tb_2O_3 ceramics.

The wavelength dependence of Verdet constant of Tb_2O_3 ceramics is shown in Figure 8 (green dot for the polarization stepping method and red circle for the probe laser sources), and the approximation fitting line in the form of $V = \frac{1}{a(\lambda^2 - \lambda_0^2)}$ (a = 0.00769 (T·m)/(rad·μm^2) and λ_0 = 299 nm) is displayed by a red dashed line. In addition, the approximation V(λ) of a TGG crystal is shown in Figure 8 by a black circle as a comparison [58]. The prepared Tb_2O_3 ceramics present three times larger values of the Verdet constant than those of TGG single crystals in the entire measured wavelength range. The magnetic field value at the center of the magnet system obeys the law $H \sim ln(D/d)$; there, D and d are the external and internal diameter of the magnetic system. Using a magneto-optical element of the same length and diameter with a Verdet constant three times greater will reduce the magnitude of the H by the same amount, resulting in a magnet volume/mass/cost reduction of more than 10 times for standard magnetic systems due to the logarithmic law. Concerning the transmittance bands in the visible to near-infrared region, Tb_2O_3 ceramics are promising alternative materials of TGG single crystals and can be competitively applied in Faraday devices operating in visible and ~1 μm (lasers based on Yb and Nd doped materials).
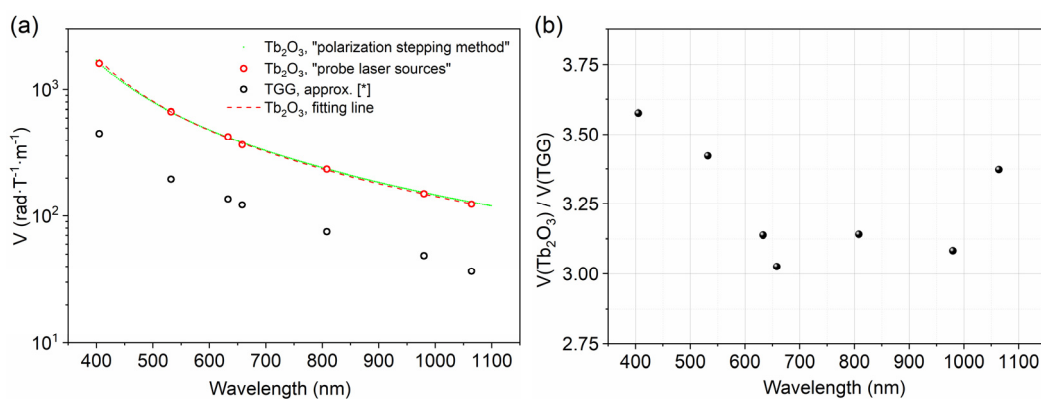

Figure 8. Wavelength dependence of Verdet constant of Tb_2O_3 ceramics (green dot and red circle) and TGG single crystal (black circle) [58] (**a**), V(Tb_2O_3)/V(TGG) ratio versus wavelength (**b**).

4. Conclusions

White Tb_2O_3 powder with the average crystalline size of 59 nm and the average particle size of 135 nm was successfully prepared via the liquid precipitation method with subsequent reduction in the NH_3 flow for the first time. Tb_2O_3 transparent ceramics were fabricated by the two-step sintering method containing vacuum pre-sintering and HIP post-treatment at relative low temperatures from the as-synthesized Tb_2O_3 powder. The Tb_2O_3 ceramics with the thickness of 1.0 mm present high values of in-line transmittance: 79.4% at 1400 nm, 78.1% at 1064 nm, and 70.3% at 633 nm, respectively. The microstructure of the Tb_2O_3 ceramics appears virtually dense, with a tiny amount of residual nano-size pores and the average grain size of approximately 1.3 μm. These pores result in the decrease in the in-line transmittance in the short-wavelength regions. The future work on the increase in optical quality will concentrate on the removal of the residual nano-size pores with both the improvement of the sintering conditions and the optimization of the synthesized Tb_2O_3 nano-powder. The wavelength dependence of the Verdet constant of the obtained Tb_2O_3 ceramics was studied in 405–1064 nm ($V = -427.3$ rad·T^{-1}·m^{-1} at 633 nm and $V = -123.7$ rad·T^{-1}·m^{-1} at 1064 nm) at room temperature. The Verdet constant of Tb_2O_3 ceramics is about three times larger than that of TGG materials in the measured visible to near-infrared range, especially, it is about 3.4 times larger than TGG single crystals at the concerned 1064 nm. The high transparency and large Verdet constant make Tb_2O_3 transparent ceramics more advantageous and competitive for a Faraday isolator used in the visible to near-infrared region.

Author Contributions: Conceptualization, methodology and investigation, J.L. and D.H.; validation, X.L. and P.C.; formal analysis, writing—original draft preparation and visualization, D.H. and L.Z.; writing—review and editing, Z.D. and I.S.; supervision, J.L., O.P. and S.B.; resources, project administration and funding acquisition, J.L. All authors have read and agreed to the published version of the manuscript.

Institutional Review Board Statement: Not applicable.

Informed Consent Statement: Not applicable.

Data Availability Statement: Not applicable.

Conflicts of Interest: The authors declare no conflict of interest.

References

1. Freiser, M. A survey of magnetooptic effects. *IEEE Trans. Magn.* **1968**, *4*, 152–161. [CrossRef]
2. Pershan, P.S. Magneto-optical effects. *J. Appl. Phys.* **1967**, *38*, 1482–1490. [CrossRef]
3. Castera, J.; Hepner, G. Isolator in integrated optics using Faraday and Cotton-Mouton effects. *Appl. Opt.* **1977**, *16*, 2031–2033. [CrossRef] [PubMed]
4. Kumari, S.; Chakraborty, S. Study of different magneto-optic materials for current sensing applications. *J. Sens. Sens. Syst.* **2018**, *7*, 421–431. [CrossRef]
5. Dai, J.W.; Li, J. Promising magneto-optical ceramics for high power Faraday isolators. *Scr. Mater.* **2018**, *155*, 78–84. [CrossRef]
6. Carothers, K.J.; Norwood, R.A.; Pyun, J. High Verdet constant materials for magneto-optical Faraday rotation: A review. *Chem. Mater.* **2022**, *34*, 2531–2544. [CrossRef]
7. Aplet, L.J.; Carson, J.W. A Faraday effect optical isolator. *Appl. Opt.* **1964**, *3*, 544–545. [CrossRef]
8. Stadler, B.J.H.; Mizumoto, T. Integrated magneto-optical materials and isolators: A review. *IEEE Photonics J.* **2014**, *6*, 1–15. [CrossRef]
9. Borrelli, N.F. Faraday rotation in glasses. *J. Chem. Phys.* **1964**, *41*, 3289–3293. [CrossRef]
10. Berger, S.B.; Rubinstein, C.B.; Kurkjian, C.R.; Treptow, A.W. Faraday rotation of rare-earth (III) phosphate glasses. *Phys. Rev.* **1964**, *133*, A723–A727. [CrossRef]

11. Dillon, J.F. Origin and uses of the Faraday rotation in magnetic crystals. *J. Appl. Phys.* **1968**, *39*, 922–929. [CrossRef]
12. Xue, Y.L.; Zhu, F.; Wang, J.; Sun, S.Y.; Hu, L.L.; Tang, D.Y. Fabrication and comprehensive structural and spectroscopic properties of Er:Y_2O_3 transparent ceramics. *J. Rare Earth*, 2021; in press. [CrossRef]
13. Yang, C.L.; Huang, J.Q.; Huang, Q.F.; Deng, Z.H.; Wang, Y.Y.; Li, X.Y.; Zhou, Z.H.; Chen, J.; Liu, Z.G.; Guo, W. Optical, thermal, and mechanical properties of $(Y_{1-x}Sc_x)_2O_3$ transparent ceramics. *J. Adv. Ceram.* **2022**, *11*, 901–911. [CrossRef]
14. Li, J.; Dai, J.W.; Pan, Y.B. Research progress on magneto-optical transparent ceramics. *J. Inorg. Mater.* **2018**, *33*, 1–8. [CrossRef]
15. Kagan, M.A.; Khazanov, E.A. Thermally induced birefringence in Faraday devices made from terbium gallium garnet-polycrystalline ceramics. *Appl. Opt.* **2004**, *43*, 6030–6039. [CrossRef]
16. Yasuhara, R.; Tokita, S.; Kawanaka, J.; Kawashima, T.; Kan, H.; Yagi, H.; Nozawa, H.; Yanagitani, T.; Fujimoto, Y.; Yoshida, H.; et al. Cryogenic temperature characteristics of Verdet constant on terbium gallium garnet ceramics. *Opt. Express* **2007**, *15*, 11255–11261. [CrossRef]
17. Yoshida, H.; Tsubakimoto, K.; Fujimoto, Y.; Mikami, K.; Fujita, H.; Miyanaga, N.; Nozawa, H.; Yagi, H.; Yanagitani, T.; Nagata, Y.; et al. Optical properties and Faraday effect of ceramic terbium gallium garnet for a room temperature Faraday rotator. *Opt. Express* **2011**, *19*, 15181–15187. [CrossRef]
18. Feng, Y.; Lin, H.; Chen, C.; Yi, X.Z.; Tang, Y.R.; Zhang, S.; Yu, T.; Chen, W.; Zhou, S.M. Fabrication of transparent $Tb_3Ga_5O_{12}$ ceramic. *Chin. Opt. Lett.* **2015**, *13*, 31602–31605. [CrossRef]
19. Ikesue, A.; Aung, Y.L. Magneto-optic transparent ceramics. In *Processing of Ceramics: Breakthrough in Optical Ceramics*; Ikesue, A., Ed.; John Wiley & Sons: Hoboken, NJ, USA, 2021; pp. 143–185. [CrossRef]
20. Li, X.Y.; Snetkov, I.L.; Yakovlev, A.; Liu, Q.; Liu, X.; Liu, Z.Y.; Chen, P.H.; Zhu, D.Y.; Wu, L.X.; Yang, Z.X.; et al. Fabrication and performance evaluation of novel transparent ceramics RE:$Tb_3Ga_5O_{12}$ (RE = Pr, Tm, Dy) toward magneto-optical application. *J. Adv. Ceram.* **2021**, *10*, 271–278. [CrossRef]
21. Lin, H.; Zhou, S.M.; Teng, H. Synthesis of $Tb_3Al_5O_{12}$ (TAG) transparent ceramics for potential magneto-optical applications. *Opt. Mater.* **2011**, *33*, 1833–1836. [CrossRef]
22. Chen, C.; Zhou, S.M.; Lin, H.; Yi, Q. Fabrication and performance optimization of the magneto-optical $(Tb_{1-x}R_x)_3Al_5O_{12}$(R = Y, Ce) transparent ceramics. *Appl. Phys. Lett.* **2012**, *101*, 131908. [CrossRef]
23. Furuse, H.; Yasuhara, R.; Hiraga, K.; Zhou, S.M. High Verdet constant of Ti-doped terbium aluminum garnet (TAG) ceramics. *Opt. Mater. Express* **2016**, *6*, 191–196. [CrossRef]
24. Aung, Y.L.; Ikesue, A. Development of optical grade $(Tb_xY_{1-x})_3 Al_5 O_{12}$ ceramics as Faraday rotator material. *J. Am. Ceram. Soc.* **2017**, *100*, 4081–4087. [CrossRef]
25. Dai, J.W.; Pan, Y.B.; Xie, T.F.; Kou, H.M.; Li, J. Highly transparent $Tb_3Al_5O_{12}$ magneto-optical ceramics sintered from co-precipitated powders with sintering aids. *Opt. Mater.* **2018**, *78*, 370–374. [CrossRef]
26. Li, X.Y.; Liu, Q.; Liu, X.; Zhu, D.Y.; Hu, D.J.; Tian, F.; Wu, L.X.; Yang, Z.X.; Xie, T.F.; Chen, H.H.; et al. Sintering parameter optimization of $Tb_3Al_5O_{12}$ magneto-optical ceramics by vacuum sintering and HIP post-treatment. *J. Am. Ceram. Soc.* **2021**, *104*, 2116–2124. [CrossRef]
27. Chen, J.; Tang, Y.; Chen, C.; Hao, D.M.; Yi, X.Z.; Ao, G.; Tian, Y.N.; Zhou, S.M. Roles of zirconia-doping in the sintering process of high quality $Tb_3Al_5O_{12}$ magneto-optic ceramics. *Scr. Mater.* **2020**, *176*, 83–87. [CrossRef]
28. Snetkov, I.L.; Permin, D.A.; Balabanov, S.S.; Palashov, O.V. Wavelength dependence of Verdet constant of Tb^{3+}:Y_2O_3 ceramics. *Appl. Phys. Lett.* **2016**, *108*, 161905. [CrossRef]
29. Ikesue, A.; Aung, Y.L.; Makikawa, S.; Yahagi, A. Polycrystalline $(Tb_XY_{1-X})_2O_3$ Faraday rotator. *Opt. Lett.* **2017**, *42*, 4399–4401. [CrossRef]
30. Ikesue, A.; Aung, Y.L.; Makikawa, S.; Yahagi, A. Total performance of magneto-optical ceramics with a bixbyite structure. *Materials* **2019**, *12*, 421. [CrossRef]
31. Balabanov, S.S.; Permin, D.A.; Rostokina, E.Y.; Palashov, O.V.; Snetkov, I.L. Characterizations of REE:Tb_2O_3 magneto-optical ceramics. *Phys. Status Solidi B* **2020**, *257*, 1900474. [CrossRef]
32. Zhang, J.Y.; Chen, H.T.; Wang, J.P.; Wang, D.W.; Han, D.; Zhang, J.; Wang, S.W. Preparation of $(Tb_{1-x}Lu_x)_2O_3$ transparent ceramics by solid solution for magneto-optical application. *J. Eur. Ceram. Soc.* **2020**, *41*, 2818–2825. [CrossRef]
33. Furuse, H.; Yasuhara, R. Magneto-optical characteristics of holmium oxide (Ho_2O_3) ceramics. *Opt. Mater. Express* **2017**, *7*, 827–833. [CrossRef]
34. Vojna, D.; Yasuhara, R.; Furuse, H.; Slezak, O.; Hutchinson, S.; Lucianetti, A.; Mocek, T.; Cech, M. Faraday effect measurements of holmium oxide (Ho_2O_3) ceramics-based magneto-optical materials. *High Power Laser Sci. Eng.* **2018**, *6*, E2. [CrossRef]
35. Lu, B.; Cheng, H.M.; Xu, X.X.; Chen, H.B. Preparation and characterization of transparent magneto-optical Ho_2O_3 ceramics. *J. Am. Ceram. Soc.* **2019**, *102*, 118–122. [CrossRef]
36. Balabanov, S.; Filofeev, S.; Ivanov, M.; Kaigorodov, A.; Kuznetsov, D.; Hu, D.J.; Li, J.; Palashov, O.; Permin, D.; Rostokina, E.; et al. Fabrication and characterizations of holmium oxide based magneto-optical ceramics. *Opt. Mater.* **2020**, *101*, 109741. [CrossRef]
37. Hu, D.J.; Li, X.Y.; Snetkov, I.; Yakovlev, A.; Balabanov, S.; Ivanov, M.; Liu, X.; Liu, Z.Y.; Tian, F.; Xie, T.F.; et al. Fabrication, microstructure and optical characterizations of holmium oxide (Ho_2O_3) transparent ceramics. *J. Eur. Ceram. Soc.* **2020**, *41*, 759–767. [CrossRef]
38. Morales, J.R.; Amos, N.; Khizroev, S.; Garay, J.E. Magneto-optical Faraday effect in nanocrystalline oxides. *J. Appl. Phys.* **2011**, *109*, 093110. [CrossRef]

39. Snetkov, I.L.; Yakovlev, A.I.; Permin, D.A.; Balabanov, S.S.; Palashov, O.V. Magneto-optical Faraday effect in dysprosium oxide (Dy_2O_3) based ceramics obtained by vacuum sintering. *Opt. Lett.* **2018**, *43*, 4041–4044. [CrossRef]

40. Aung, Y.L.; Ikesue, A.; Yasuhara, R.; Iwamoto, Y. Magneto-optical Dy_2O_3 ceramics with optical grade. *Opt. Lett.* **2020**, *45*, 4615–4617. [CrossRef]

41. Zhou, D.; Li, X.H.; Wang, T.; Xu, J.Y.; Wang, Z.Y.; Shi, Y.; Permin, D.; Balabanov, S.S. Fabrication and magneto-optical property of $(Dy_{0.7}Y_{0.25}La_{0.05})_2O_3$ transparent ceramics by PLSH technology. *Magnetochemistry* **2020**, *6*, 70. [CrossRef]

42. Balabanov, S.; Filofeev, S.; Kaygorodov, A.; Khrustov, V.; Kuznetsov, D.; Novikova, A.; Permin, D.; Popov, P.; Ivanov, M. Hot pressing of Ho_2O_3 and Dy_2O_3 based magneto-optical ceramics. *Opt. Mater. X* **2022**, *13*, 100125. [CrossRef]

43. Veber, P.; Velázquez, M.; Gadret, G.; Rytz, D.; Peltz, M.; Decourt, R. Flux growth at 1230 °C of cubic Tb_2O_3 single crystals and characterization of their optical and magnetic properties. *CrystEngComm* **2014**, *17*, 492–497. [CrossRef]

44. Yang, M.Q.; Zhou, D.; Xu, J.Y.; Tian, T.; Jia, R.P.; Wang, Z.Y. Fabrication and magneto-optical property of yttria stabilized Tb_2O_3 transparent ceramics. *J. Eur. Ceram. Soc.* **2019**, *39*, 5005–5009. [CrossRef]

45. Zhang, J.Y.; Chen, H.T.; Wang, J.P.; Wang, D.W.; Han, D.; Zhang, J.; Wang, S.W. Phase transformation process of Tb_2O_3 at elevated temperature. *Scr. Mater.* **2019**, *171*, 108–111. [CrossRef]

46. Balabanov, S.S.; Permin, D.A.; Rostokina, E.Y.; Egorov, S.V.; Sorokin, A.A.; Kuznetsov, D.D. Synthesis and structural characterization of ultrafine terbium oxide powders. *Ceram. Int.* **2017**, *43*, 16569–16574. [CrossRef]

47. Yakovlev, A.; Balabanov, S.; Permin, D.; Ivanov, M.; Snetkov, I. Faraday rotation in erbium oxide based ceramics. *Opt. Mater.* **2020**, *101*, 109750. [CrossRef]

48. Sun, Z.G.; Chen, Z.Y.; Wang, M.Y.; Lu, B. Production and optical properties of Ce^{3+}-activated and Lu^{3+}-stabilized transparent gadolinium aluminate garnet ceramics. *J. Am. Ceram. Soc.* **2019**, *103*, 809–818. [CrossRef]

49. Hu, D.J.; Liu, X.; Liu, Z.Y.; Li, X.Y.; Tian, F.; Zhu, D.Y.; Yang, Z.X.; Wu, L.X.; Li, J. Fabrication of Dy_2O_3 transparent ceramics by vacuum sintering using precipitated powders. *Magnetochemistry* **2020**, *7*, 6. [CrossRef]

50. Runde, W.; Meinrath, G.; Kim, J.I. A study of solid-liquid phase equilibria of trivalent lanthanide and actinide ions in carbonate systems. *Radiochim. Acta* **1992**, *58/59*, 93–100. [CrossRef]

51. Happy; Tok, A.I.; Su, L.T.; Boey, F.Y.C.; Ng, S.H. Homogeneous precipitation of Dy_2O_3 nanoparticles—Effects of synthesis parameters. *J. Nanosci. Nanotechnol.* **2007**, *7*, 907–915. [CrossRef]

52. Salavati-Niasari, M.; Javidi, J.; Davar, F.; Fazl, A.A. Sonochemical synthesis of $Dy_2(CO_3)_3$ nanoparticles and their conversion to Dy_2O_3 and $Dy(OH)_3$: Effects of synthesis parameters. *J. Alloys Compd.* **2010**, *503*, 500–506. [CrossRef]

53. Caro, P.; Sawyer, J.; Evning, L. The infrared spectra of rare earth carbonates. *Spectrochim. Acta A Mol. Spectrosc.* **1972**, *28*, 1167–1173. [CrossRef]

54. Zhang, J.; Von Dreele, R.; Eyring, L. The structures of Tb_7O_{12} and $Tb_{11}O_{20}$. *J. Solid State Chem.* **1993**, *104*, 21–32. [CrossRef]

55. Balabanov, S.S.; Permin, D.A.; Rostokina, E.Y.; Egorov, S.V.; Sorokin, A.A. Sinterability of nanopowders of terbia solid solutions with scandia, yttria, and lutetia. *J. Adv. Ceram.* **2018**, *7*, 362–369. [CrossRef]

56. Monshi, A.; Foroughi, M.R.; Monshi, M.R. Modified scherrer equation to estimate more accurately nano-crystallite size using XRD. *World J. Nano Sci. Eng.* **2012**, *2*, 154–160. [CrossRef]

57. Mollaee, M.; Zhu, X.; Jenkins, S.; Zong, J.; Temyanko, E.; Norwood, R.; Chavez-Pirson, A.; Li, M.; Zelmon, D.; Peyghambarian, N. Magneto-optical properties of highly Dy^{3+} doped multicomponent glasses. *Opt. Express* **2020**, *28*, 11789–11796. [CrossRef]

58. Snetkov, I.L.; Yasuhara, R.; Starobor, A.V.; Mironov, E.A.; Palashov, O.V. Thermo-optical and magneto-optical characteristics of terbium scandium aluminum garnet crystals. *IEEE J. Quantum Electron.* **2015**, *51*, 1–7. [CrossRef]